

Disclaimer/Publisher's Note: The statements, opinions, and data contained in all publications are solely those of the individual author(s) and contributor(s) and not of MDPI and/or the editor(s). MDPI and/or the editor(s) disclaim responsibility for any injury to people or property resulting from any ideas, methods, instructions, or products referred to in the content.

# Numerical Investigation into the Influence of Alloy Type and Thermo-mechanics on Void Formation in Friction Stir Welding of Aluminium Alloys

Mohammad Ali Ansari, Hemant Agiwal, Daniel Franke, Mike Zinn, Frank E. Pfefferkorn, Shiva Rudraraju\*

Department of Mechanical Engineering, University of Wisconsin-Madison, Madison, Wisconsin, USA

\* Corresponding author (shiva.rudraraju@wisc.edu)

## Abstract:

This study employs a high-fidelity numerical framework to determine the plastic material flow patterns and temperature distributions that lead to void formation during friction stir welding (FSW), and to relate the void morphologies to the underlying alloy material properties and process conditions. Three aluminum alloys, viz., 6061-T6, 7075-T6, and 5053-H18 were investigated under varying traverse speeds. The choice of aluminum alloys enables investigation of a wide range of thermal and mechanical properties. The numerical simulations were validated using experimental observations of void morphologies in these three alloys. Temperatures, plastic strain rates, and material flow patterns are considered. The key results from this study are: (1) The predicted stir zone and void morphology are in good agreement with the experimental observations, (2) The temperature and plastic strain-rate maps in the steady-state process conditions show a strong dependency on the alloy type and traverse speeds, (3) The material velocity contours provide a good insight into the material flow in the stir zone for the FSW process conditions that result in voids as well as those that do not result in voids. The numerical model and the ensuing parametric studies presented in this work provide a framework for understanding material flow under different process conditions in aluminum alloys, and potentially in other alloys. Furthermore, the utility of the numerical model for making quantitative predictions and investigating different process parameters to reduce void formation is demonstrated.

**Keywords:** aluminum; finite element analysis; predictive model; numerical analysis; voids; material flow; plasticity

## 1. Introduction

Friction stir welding (FSW) is a solid-state joining process invented by The Welding Institute (TWI) in the United Kingdom in 1991[1]. During FSW, a non-consumable rotating tool penetrates the workpiece and is traversed over a weld seam to produce a joint. High strain rates combined with frictional heating and axial pressure from the tool lead to plastic deformation of the material whilst maintaining sub-solidus processing temperatures. The plastically deformed material is intermixed around the tool geometry leading to a refined grain structure in the stirred zone [2,3]. The solid-state nature of the process provides FSW significant advantages over conventional fusion-based welding technologies, including the absence of porosity, hot cracks, distortion, and other melting-related defects [4]. The improved microstructure provides the weldment with superior mechanical and corrosion performance over fusion welded parts. FSW also allows for the processing and joining of difficult-to-weld materials such as aluminum and magnesium alloys. With numerous advantages of FSW, the technology faces limitations with respect to large process forces, overhead costs, tool wear, low production rates, and weld geometry restrictions. A schematic of the FSW process is shown in Figure 1.



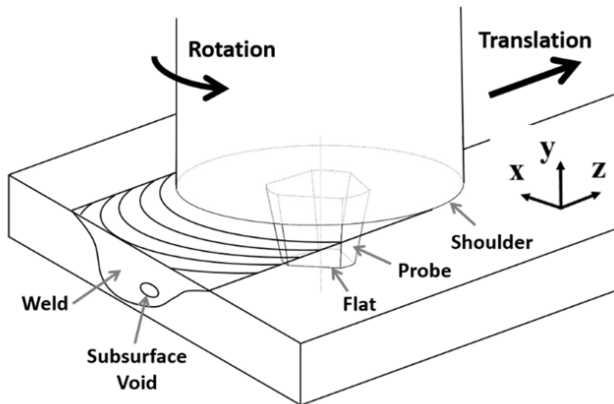


Figure 1: Schematic of the FSW process. The translational and rotational motion of the tool relative to the workpiece leads to a shearing action on the material by the tool probe. This creates a plastic stir zone that forges the deformed material behind the tool probe. Suboptimal process conditions can potentially lead to defective welds with subsurface voids.

The flow of plastically deformed material around the tool probe plays a critical role in the weld quality during FSW. The shearing action of the tool probe extrudes the plastically deformed material in front of the probe and successively forges the deformed material behind the probe as the tool moves in the welding direction. The processing conditions play a critical role in the consolidation of the deformed material in the weld zone. Unsuitable choice of process parameters, including rotational and traverse speed [5,6], probe geometry [7,8], tool's shoulder diameter [9], and tool's tilt angle [10], might cause inefficient material flow and inappropriate temperature distribution around the tool. Consequently, defects form due to excessive or insufficient heat input as well as abnormal stirring during FSW [11]. Broadly, there are three types of topological defects caused in the welded specimens in terms of spatial distribution because of insufficient heat flow and/or plastic material flow. When the plastically deformed material is not sufficient to consolidate in the cavity generated by the FS probe's advance per revolution, it leaves a void behind the trailing edge of the probe. When the processing conditions are such that a void is formed with the probe's every revolution, it leaves a continuous tunnel defect. A void or tunnel defect is limited to the probe-driven region of the weld zone. When the defect extends to the shoulder-driven region and extends all the way to the surface of the weld, it's termed a groove defect [12,13]. Due to the nature of probe movement, these defects are dominantly seen on the advancing side of the probe. On the contrary, excessive heat input can also produce defective FSW specimens. Considerably high rotational and low traverse speeds can lead to excessive deformation of the material around the tool shoulder. When the tool shoulder is unable to confine this deformed material, the excessive material escapes out as a flash, resulting in thinner stir zones and reduced mechanical properties. Figure 2 shows some of these defect morphologies, as observed in FSW experiments. Subsurface defect detection continues to be a foremost challenge during FSW. Post-weld inspections are costly and time-consuming. Non-destructive and real-time monitoring techniques for the detection of defects are gathering interest.

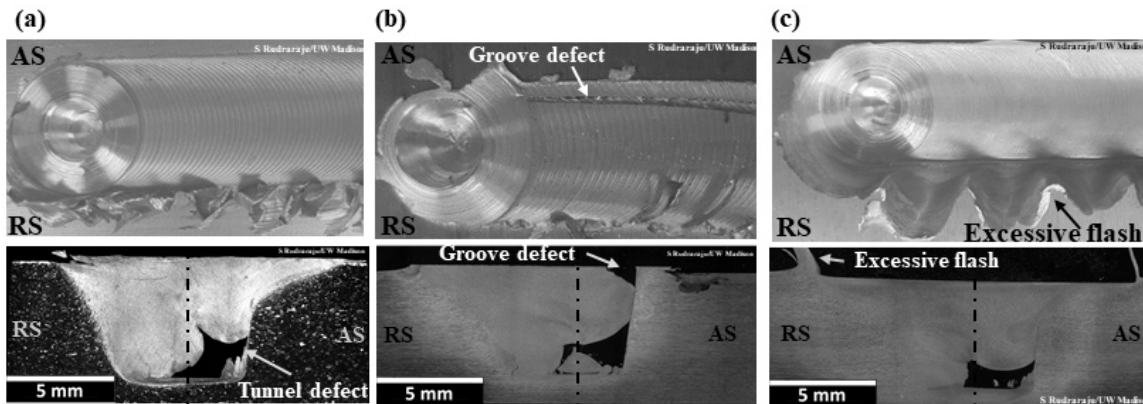


Figure 2: Top and cross-section view image of different defects during FSW (a) tunnel defect, (b) groove-like defect, and (c) excessive flash (AS-advancing side; RS-retreating side)

In a recent study by the authors of this manuscript, defect formation and material flow during FSW of aluminum 6061 alloys were observed using high-speed high-energy synchrotron X-ray beams [14]. In this first-of-its-kind experimental setup, the author's captured the density changes using high-intensity X-ray beams that showed the periodic formation and filling of the cavity behind the tool probe. Other methods, such as the use of eddy currents [15] and force-based defect monitoring [16,17], have also been implemented successfully. Particularly, attention is drawn to a very recent study by the authors [23] linking some of these defect morphologies with the variations in the reaction force felt by the tool. While in that work, we looked at the interaction of the defect with the tool probe and the reaction forces produced by the tool probe-defect interaction, in the current manuscript we look at the material flow and thermo-mechanics aspects. Our aim here is to relate the workpiece temperature distribution and material flow variations of different alloys of a given material (Aluminium in this work) to the resulting defect morphologies.

Through recent publications, numerical modeling has proved to be a powerful tool to create a fundamental understanding of the material flow and thermomechanical transformations during FSW and understand defect formation mechanisms. Various numerical frameworks have been proposed in the literature with varying degrees of numerical fidelity (mesh resolution, mesh movement, material flow resolution, time step resolution, etc.) and physics fidelity (thermomechanical material properties and boundary conditions, contact modeling, void representations, etc.). Eulerian (fixed in space) framework-based computational fluid dynamics (CFD) and Lagrangian (attached to the material) framework-based computational solid mechanics (CSM) are the most-accepted choices for modeling material flow for solid-state processes. However, recent computational studies have focused on combining these two frameworks, yielding the constructs of coupled Eulerian-Lagrangian (CEL) method and arbitrary Lagrangian-Eulerian (ALE) method. Schmidt and Hattel [18] simulated the plasticized stir zone and weld voids using the ALE framework. To avoid the high computational cost of the ALE formulations and the incapability of CFD frameworks towards predicting plasticity and void formation, the CEL framework is being widely used in recent literature and hence is also adopted in this current study. CEL enables better modeling of the material flow, formation of plasticized stir zone, and different types of voids that might occur during FSW. Al-Badour et al. [19] developed a CEL formulation to explore the effect of the coefficient of friction and process parameters on weld quality and void formation. Zhu et al. [20] have used the same framework to investigate the probe geometry and its effect on material flow during FSW. They showed that the probe feature has a substantial impact on weld quality. Dialami et al. [21] created a numerical framework based on ALE and CEL stages, and by adding a particle tracing strategy, this framework could simulate defects like joint line remnants.

Ajri and Shin [22] have simulated different voids, including cavity, tunnel, groove-like, and excess flash formation, using the CEL framework.

*This manuscript is part of a two-part study looking into the interaction of voids with the tool probe and the underlying material flow. The first study, involving void-tool interactions and the novel reaction force signatures observed, that are shown to be useful in remote void detection, has been recently published by the authors [23] in this journal. In this second study, the authors use a similar high-fidelity numerical framework to study the impact of alloy type on material flow and void formation.* This study focusses on three different aluminum alloys, viz., Al-6061-T6, Al-5083-H18, and Al-7075-T6, with varying process parameters. As shown in this manuscript, variations in the void morphology, temperature distribution, and strain distribution across the three alloys provide significant insights into the effect of temperature dependent plastic deformation specific to each alloy on their void forming propensity. The numerical predictions were validated by performing FSW experiments and comparing numerical void morphologies to experimental cross-sectional micrographs of voids. To the author's best knowledge, such a numerical study of the effect of alloy type on void formation has not been sufficiently explored in the literature.

## 2. Experimental setup

FSW experiments were performed on a three-axis CNC mill (HAAS TM-1) in position control mode. FSW was performed on three different aluminum alloy workpieces (6061-T6, 7075-T6, and 5083-H18), with all plates of dimensions 200 mm x 100 mm x 6 mm. All experiments were performed using an FS tool made of hardened H13 tool steel, consisting of a 15-mm-diameter concave shoulder and a 5.2-mm-long conical probe tapering from 6.3-mm-diameter at the shoulder to 5 mm at the tip. All 120-mm-long FSW tests were performed with a 0° travel angle using a 6.35 mm thick mild steel backing plate. A spindle rotational speed of 900 RPM was used for all experiments, along with a constant plunging speed of 25 mm/min and commanded plunge depth of 0.2 mm. Traverse speeds of 60 mm/min, 300 mm/min, and 600 mm/min was used for producing welds across defective and non-defective regimes. All tests were performed with both the workpiece and tool at room temperature, and multiple repetitions were performed for consistency.

Table 1 lists the experimental parameters needed to create the defective and non-defective welds explored in this study. Process forces during FSW were measured by placing the workpieces atop a three-axis piezo-electric dynamometer (Kistler model 9265). Signals from the dynamometer were guided to the charge amplifiers to read the forces by the DAQ system (National Instruments, BNC-2090A, PCI-6014, PCIe-6320).

Table 1:Process parameters for the FSW experiments in this study

Test	Aluminum alloy	Rotational speed (rpm)	Traverse speed (mm/min)
1-3	Al-6061		60, 300, 600
4-6	Al-7075	900	60, 300, 600
7-9	Al-5083		60, 300, 600

The average steady-state forces have been reported and analyzed in this study. Post-process characterization of welded specimens was performed by cross-sectioning the specimens perpendicular to the traverse direction (X-Y) in the steady state regimen. The cross-sections were ground, polished, and etched to reveal the stir zone. For Al-7075-T6 and Al-5083-H18, Keller's reagent was used,

whereas modified Poulton's reagent was used for Al-6061-T6. The prepared cross-sections were observed under a white light optical microscopy system (Alicona Infinite Focus).

### 3. Numerical Framework

We adopt a finite element method (FEM) framework for solving the governing equations of mechanical equilibrium, heat conduction and contact mechanics that are required in modeling the FSW process. The FSW process and the associated material deformation, thermos-mechanics, and contact mechanics can be effectively treated in a Coupled Eulerian-Lagrangian (CEL) framework of FEM. This framework is available within the ABAQUS Explicit Finite Element package [40].

To reduce the processing time, the proposed numerical model skipped the plunging and dwelling phase, given the slower feed rates of plunge during the FSW process. The volume fraction of the Eulerian domain was defined using a reference domain. The reference domain has empty space with the same probe and shoulder depression geometry at the center, and the rest of the reference domain is the solid material. Since a plunging and dwelling phase of the process was not modeled, the initial startup of the process is non-physical. To avoid any overestimations due to the non-physical startup, the numerical results were only investigated when the process's lateral and transitional forces reached a steady-state condition. Figure 3 (a) shows the Eulerian cube shape domain with a volume of  $25 \times 80 \times 9 \text{ mm}^3$ . Eulerian domain included two main regions: The blue zone (full region) was assigned to the aluminum alloy with a thickness of 6 mm (same as the thickness of the experimental plate). In the red zone (void region), no material was assigned, which shows the empty space of the tool at the center and an extra 3 mm empty space at the top of the workpiece into which material can displace (e.g., flash). In a typical example, the Eulerian body is meshed with 24,948 thermally coupled Eulerian elements (EC3D8RT) with a size of 1 mm, having four degrees of freedom per node. The meshed FS tool and the tool reference point are presented in Figure 3 (b). The tool is modeled using Lagrangian rigid body formulation consisting of 14060 4-node thermally coupled tetrahedron (C3D4T) elements with a size of 1 mm. The FS tool dimension and geometry are the same as the tool used in physical experiments.

Because the FS tool was modeled as the rigid Lagrangian body, tool rotational movement and other physical properties (including mass and moment) were assigned to the tool reference point (Figure 4). The tool movement condition includes rotational speed around its local axis with no other movement along the other axes. Because the Eulerian domain is a cube, velocity constraints were assigned to the external surfaces to remove material escape from the bottom and sides of the domain. The welding phase was modeled by the inflow and outflow velocity constraints at the leading edge and trailing edge of the domain. The inflow and outflow velocity were set to the traverse speed of the welding process.

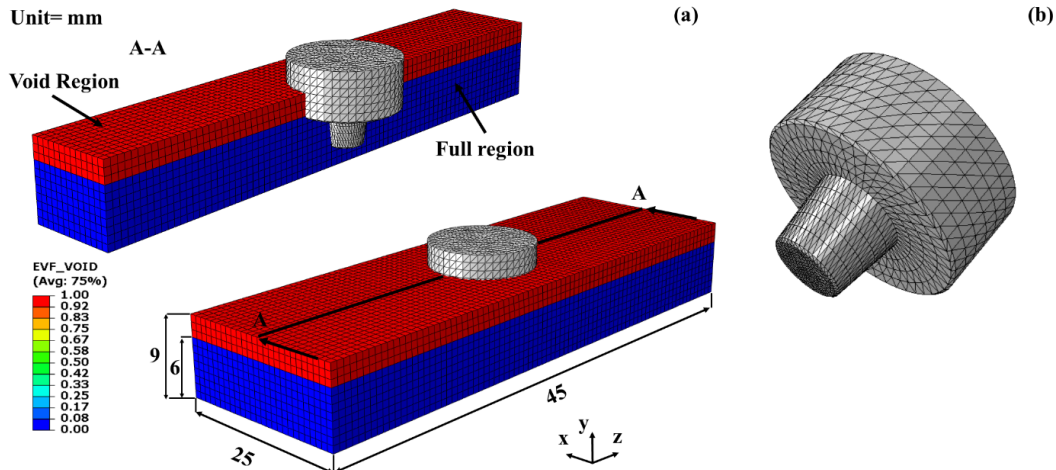


Figure 3: The geometric domain considered in the CEL framework, showing the problem geometry and the associated numerical discretization (mesh) for the (a) workpiece, and the (b) tool.

In this framework, we only consider inelastic heat generation by material softening due to model limitations. Therefore, the adiabatic heating is considered and the heat dissipation into the surroundings is ignored. Also, 95% of plastic work was assumed to be transformed into thermal energy.

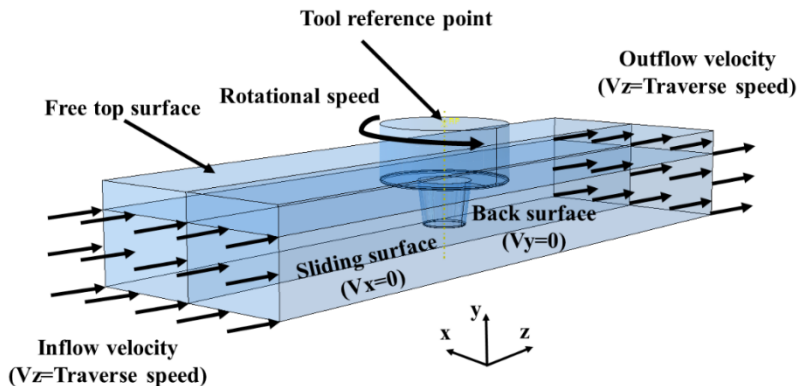


Figure 4: Boundary conditions enforced on the domain representing the workpiece.

### 3.1. Material model

Under severe deformation conditions like in FSW, material behavior is highly nonlinear under the large strain, high strain rate and close-to-solidus temperatures. The Johnson-Cook [24] empirical constitutive law is well known for modeling such strain, strain rate and temperature regimes in metals. The elasto-plastic evolution of the workpiece material, following the Johnson-Cook material model, is as follows:

$$\sigma_0 = (A + B\bar{\varepsilon}_p^n) \left( 1 + C \ln \frac{\dot{\varepsilon}_p}{\dot{\varepsilon}_0} \right) \left( 1 - \left( \frac{T - T_{ref}}{T_{melt} - T_{ref}} \right)^m \right)$$

where  $\bar{\varepsilon}_p$ ,  $\dot{\varepsilon}_p$ , and  $\dot{\varepsilon}_0$  are the effective plastic strain, the effective plastic strain rate, and the normalized strain rate, respectively. A, B, C, n, and m are material constants that are measured in a split-Hopkinson bar test, and n, m, and C are constants related to the effect of strain hardening, thermal softening, and strain rate sensitivity, respectively.  $T_{ref}$  and  $T_{melt}$  are the ambient temperature and the melting point temperature of the material, respectively.

The Johnson-Cook damage model is also used to model the damage evolution during the process. This model accounts for load path dependency by accumulating the damage in local internal variables as the deformation evolves. The scalar damage parameter D is given by the following equation.

$$\bar{\varepsilon}_f = \left( d_1 + d_2 \exp \left( d_3 \frac{p}{\bar{\sigma}} \right) \right) \left( 1 + d_4 \ln \left( \frac{\dot{\varepsilon}_p}{\dot{\varepsilon}_0} \right) \right) (1 + d_5 \bar{\theta}) \quad \& \quad D = \frac{\bar{\varepsilon}}{\bar{\varepsilon}_f}$$

Where  $d_1$  to  $d_5$ ,  $\frac{p}{\bar{\sigma}}$ ,  $\bar{\varepsilon}$ , and  $\bar{\varepsilon}_f$  are damage constant, stress triaxiality parameter, accumulative plastic strain, and fracture strain, respectively.

All aluminum alloy properties, including Johnson-Cook model parameters, Johnson-Cook damage model constant, and the thermal and elastic properties of all three alloys, are shown in Tables 2, 3, and 4, respectively [25-31]. Included are the most important temperature-dependent material properties of all the three alloys modelled in the numerical simulations, including density, thermal diffusivity, heat capacity, and elastic modulus.

To help relate the effect of the temperature dependent material properties of the three alloys on void-forming mechanisms during FSW, the mechanical strength (Ultimate tensile strength-UTS and Yield strength-YS) of these alloys ranging from room temperature to a high temperature are plotted in Figure 5(a and b) [32, 33]. Both Al-6061 and 7075 have very close UTS and YS values at a higher temperature, while Al-5083 shows higher UTS and YS values for the 150-300°C temperature range. This is believed to be due to the differences in the strengthening mechanisms active in the different alloys. Both Aluminum 6061 and Al 7075 are strengthened by precipitation-hardening heat treatment, while Al 5083 is primarily strengthened by strain hardening. Showing the difference in UTS and YS at higher temperatures can demonstrate how different materials flow under the steep gradients of thermal and deformation conditions experienced during the FSW process. It is important to note that obtaining such extensive material data for temperature dependent material properties requires collecting experimental data from varied sources in the literature, and hence, there are some gaps in the temperature ranges for some of these alloys.

Table 2. Johnson-Cook plasticity model constants

Material	A [MPa]	B [MPa]	C	n	m	T <sub>ref</sub> [°C]	T <sub>melt</sub> [°C]
Al 6061-T6 [37]	324	114	0.002	0.42	1.34	25	652
Al 7075-T6 [34]	546	678	0.059	0.72	1.56	25	635
Al 5083-H18 [36]	170	425	0.0335	0.42	1.225	25	640

Table 3. Johnson-Cook damage constants

Material	d <sub>1</sub>	d <sub>2</sub>	d <sub>3</sub>	d <sub>4</sub>	d <sub>5</sub>	̇ε <sub>0</sub>	T <sub>Transition</sub> [°C]	T <sub>melt</sub> [°C]
Al 6061-T6 [29]	-0.068	0.451	-0.952	0.036	0.697	1	25	652
Al 7075-T6 [26]	-0.068	0.451	-0.952	0.036	0.697	1	25	635
Al 5083-H18 [28]	0.0261	0.263	-0.349	0.147	16.8	1	25	640

Table 4. Temperature-dependent material properties for the three alloys

Al 6061-T6 [30]

Temp (°C)	Thermal conductivity (W/m °C)	Specific Heat (J/ kg °C)	Density (kg/m³)	Thermal Expansion (10⁻⁶/°C)	Young's modulus (GPa)	Poisson's ratio
25	162	945	2690	23.5	66.94	0.33
100	177	978	2690	24.6	63.21	0.334
149	184	1000	2670	25.7	61.32	0.335
204	192	1030	2660	26.6	56.8	0.336
260	201	1052	2660	27.6	51.15	0.338
316	207	1080	2630	28.5	47.17	0.36
371	217	1100	2630	29.6	43.51	0.4
427	229	1130	2600	30.7	28.77	0.41
482	243	1276	-	-	20.2	0.42

## Al 7075-T6 [31]

Temp (°C)	Thermal conductivity (W/m °C)	Specific Heat (J/ kg °C)	Density (kg/m³)	Thermal Expansion (10⁻⁶/°C)	Young's modulus (GPa)
25	131	750	2810	21.8	72.4
76.85	133	750	2750	22.3	71
126.85	140	840	2684	22.8	68.1
176.85	145	960	2612	23.4	63.9
226.85	152	1000	2577	24.1	58.2
276.85	157	1040	2520	24.7	49
326.85	164	1087	2457	25.2	35
376.85	169	1129	2425	25.7	20.5
426.85	176	1171	2356	26.3	16.9

## Al 5083 [27,30]

Temp (°C)	Thermal conductivity (W/m °C)	Specific Heat (J/ kg °C)	Density (kg/m³)	Temp (°C)	Thermal Expansion (10⁻⁶/°C)	Temp (°C)	Young's modulus (GPa)
25	117	924	2660	25	-	25	70
80	122.7	984.2	2640	200	25.5	100	67.8
180	131.6	1039.6	2630	300	26.8	200	60.7
280	142.3	1081.2	2610	400	28.9	250	43.1
380	152.5	1136.6	2590	500	31.5	300	42
480	159.5	1178.2	2570	-	-	350	36
580	177.2	1261.4	2550	-	-	400	26.8
-	-	-	-	-	-	450	19.4
-	-	-	-	-	-	500	14.9

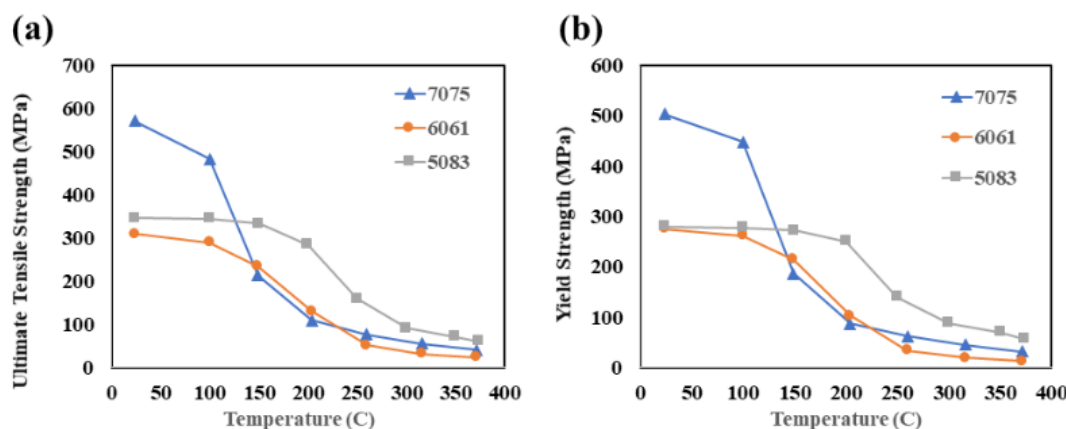


Figure 5: Temperature-dependent material properties of three aluminum alloys. (a) Ultimate Tensile Strength (MPa), and (b) Yield strength (MPa) [32, 33]

## 4. Results and discussion

### 4.1. Numerical model validation

The results from the numerical model were compared with the experimental observations of weld surface appearance, void cross-sectional morphology, and steady-state process forces. To compare the weld morphology for sub-surface defects and material flow patterns two traverse cross-sections were considered and tracked in the experimental and numerical specimens. Cross-section “A-A” (Figure 6) was created behind the trailing edge of the tool to visualize the void morphology, and cross-section “B-B” (Figure 6) was created at the trailing edge of the tool beneath the shoulder to visualize the material flow. Both cross-sections were taken in the steady-state regimen of the weld.

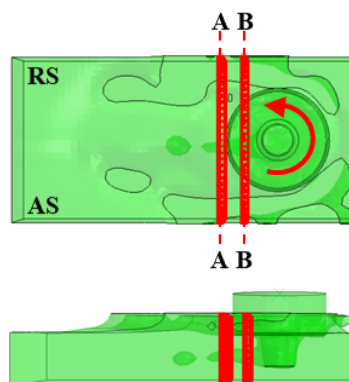


Figure 6: Workpiece cross-sections considered in the numerical model to observe process dynamics

Due to system compliance, the actual plunge reduces compared to the commanded plunge in the experiments. The maximum resemblance in the actual and commanded plunge was found when the traverse speed was lowest (60 mm/min). For this processing condition, the average steady-state forces for both experimental and numerical setups across the three alloys have been compared (Table 5). The steady-state forces are within 10% error for all three alloys suggesting strong agreement between the experiments and numerical simulations. Forces were highest for 7075-T6, followed by 5083-H18, and lowest for 6061-T6 alloy. The variation can be attributed to the different hardness of these materials, with 7075-T6 having the highest hardness and 6061-T6 being the lowest.

Table 5. Experimental and numerical steady-state axial force during the stirring phase

Aluminum	Traverse speed (mm/min)	Rotational speed (rpm)	Average Exp. steady-state force (N)	Average Num. steady-state force (N)	Error (%)
<b>6061-T6</b>			4364	4270	2.1
<b>7075-T6</b>	60	900	8148	7490	8.1
<b>5083-H18</b>			7230	6870	5.0

The weld morphology from the experimental and numerical simulation setups has been compared in Figure 7. Figure 7 (i and ii) compare the top view of the coating. There is coherence in the flash formation seen around the weld path for both setups. The flash is excessively produced on the retreating side of the weld for all alloys. The flash formation is highest for 6061-T6, followed by 7075-T6 and 5083-H18, in that order. The extent of flash formation can be attributed to the high-temperature strength of each alloy, with 5083-H18 having the highest high-temperature mechanical properties (Figure 5). The morphologies compared in this figure are for the traverse speed of 600 mm/min. At this condition,

voids were produced in all the alloys. The continuous tunnel defect in all alloys can be observed in the side view of the simulation (Figure 7-iii). These defects are observed in much depth by looking at the traverse cross-section (A-A) for both numerical and experimental setups in Figure 7-iv and v, respectively. The tunnel defect morphology is comparable in both experimental and numerical results. The size of the tunnel defect is larger in the 6061-T6 alloy compared to the 7075-T6 alloy. In the 5083-H18 alloy, the tunnel defect extended to the shoulder of the FS probe and grove is observed. For 6061-T6 and 5083-H18 alloys, the defects were dominantly situated on the advancing side of the stir zone, whereas for the 7075-T6 alloys, the void was much closer to the center of the stir zone.

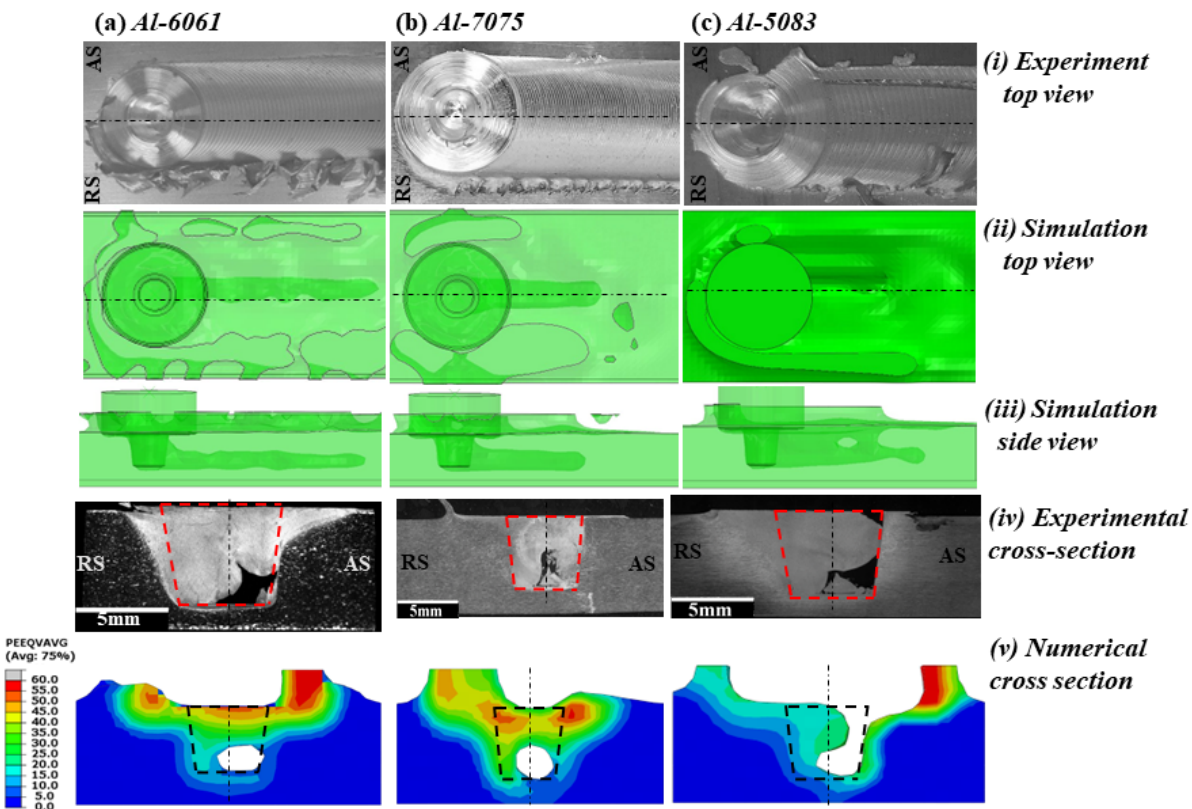


Figure 7: Comparison between experimental and numerical results for a traverse speed of 600 mm/min, for (a) Aluminum 6061-T6, (b) Aluminum 7075-T6, and (c) Aluminum 5083-H18.

#### 4.2. Effect of processing parameters on material flow and defect formation

During the FSW process for a well-consolidated bond, the processing conditions should allow for sufficient plastic material flow of the material around the tool probe. The authors have shown in a recent study that during a rotation of the FS tool probe, a cavity is formed behind the probe, which is then filled by the forging of the plastic material flow. Optimum friction surfacing conditions allow for processing temperatures of 70-90% of the solidus temperature of the workpiece material. For aluminum alloys within this temperature range, solution treatment takes place and affects the malleability of the material and leads to material softening and ease of flow [3]. Each aluminum alloy has a different as-cast property and transforms accordingly for a given processing condition. Thus, weld consolidation becomes a strong function of the process parameters and the alloy type.

For all three alloys in the study, three combinations of traverse and rotation speed were studied (

Table 1). The cross-sectional macrographs from experiments and numerical simulation are shown in Figure 8. The numerical simulations are in strong coherence with the experimental results with respect to void location and morphology, except for experiments done at 60 mm/min. In the numerical simulations, fully consolidated welds without any subsurface voids are created at 60 mm/min traverse speed for all alloys, whereas at 300 mm/min and 600 mm/min, we start observing voids. At 60 mm/min traverse speed, in contrast to the simulated results, there are smaller voids seen in the experiments. The discrepancies can be caused by the simplification of experimental setup done in the numerical frameworks through assumptions such as an absence of dynamics from the machine and tool holder (runout), the eccentricity of the tool, rigid Lagrangian body formulation for the tool, adiabatic heat effect, and constant friction coefficient. These limitations of the numerical model will be highlighted later in the discussion. However, even with the limitations of the numerical workspace, the results from the model provide coherency with the experimental observations. The void size increases with traverse speed since, for the given rotation speed, the process is getting colder, and the consolidation time for the plastically deformed material, along with the overall heat generation, reduces. As mentioned in the previous section, groove defects were observed for 5083-H18 alloys, whereas tunnel defect was observed for the rest.

To understand these variations in defect morphology with alloy and traverse speeds, the workpiece temperature distributions across the nine processing conditions are extracted from the numerical simulations and shown in Figure 9. Some general trends observed across all conditions include higher temperatures around the tool shoulder compared to the probe, a phenomenon well reported in the literature. The temperature distribution in the stir zone is asymmetric, with the retreating side hotter compared to the advancing side. The temperature variance can be attributed to the extrusion cycle of the plastically deformed material, which flows from the retreating to the advancing side [34]. As mentioned before, increasing the traverse speed leads to colder welds, and the reduction in temperature in the stir zone is visible for all three alloys.

Along with temperature, strain rate plays a crucial role in plastic deformation. The equivalent plastic strain has been demonstrated from the numerical simulations in Figure 10. The observed strain rates are of the order  $10^3$ - $10^4$  s $^{-1}$ , and these values are consistent with the literature [35, 36]. Strain rates generated during FSW are dependent on the tangential velocity of the tool and the shearing capability of the tool design. The introduction of features such as threads and flats improve the effective shearing of the surrounding material. Since, in this study, the tool has no additional features and the rotational speed of the tool is constant across all experiments, the effective strain rate is dependent on the traverse speed and alloy type. Literature has found strain rate to be inversely proportional to the weld pitch (advance of tool per revolution). The strain rates were found to increase slightly near the tool-workpiece interface for the 6061-T6 and the 7075-T6 alloys, with increasing traverse speed. Within the stir zone, the strain rate variation is similar to the temperature variation. Lower strain rates in the stir zone with higher traverse speed and higher strain rates on the retreating side were observed for both alloys. This can be potentially attributed to the increased weld pitch or the advance of the FS tool per revolution. An increased weld pitch leads to an increase in the stirred material per revolution, which can reduce the strain rates. The combined effect of strain rate and temperature drives the plastic flow during FSW. Around the probe region, a reduction in temperature and strain rates was observed, which can be correlated with the increased void size.

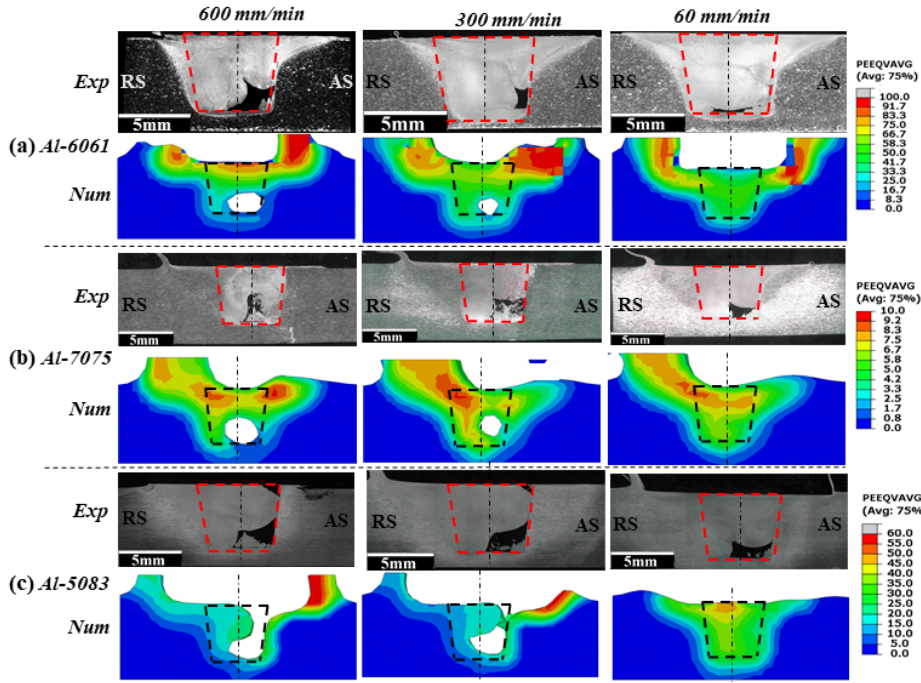


Figure 8: Void morphology observed in the numerical and experimental cross-sections at three traverse speeds for (a) Al-6061-T6, (b) Al-7075-T6, and (c) Al-5083-H18.

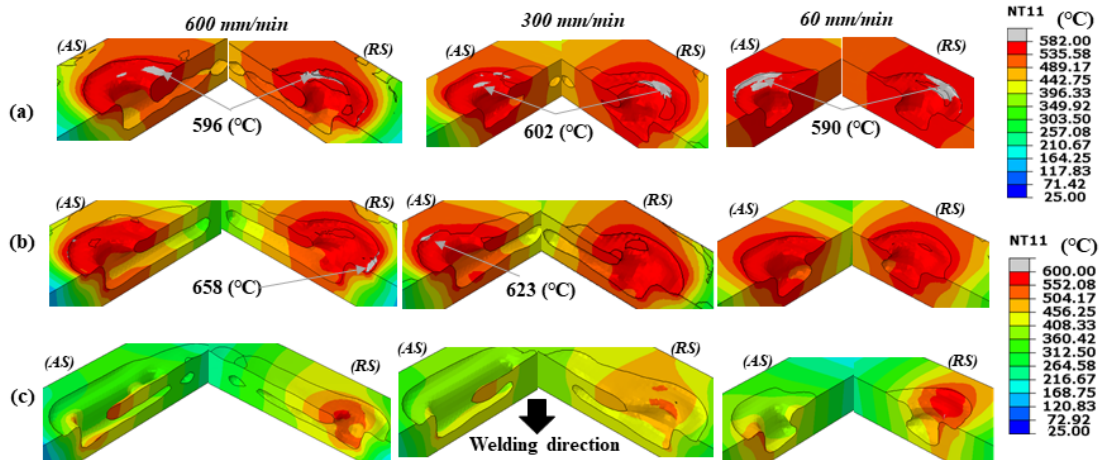


Figure 9: Temperature distribution around the tool and probe at three traverse speeds for (a) Al-6061-T6, (b) Al-7075-T6, and (c) Al-5083-H18.

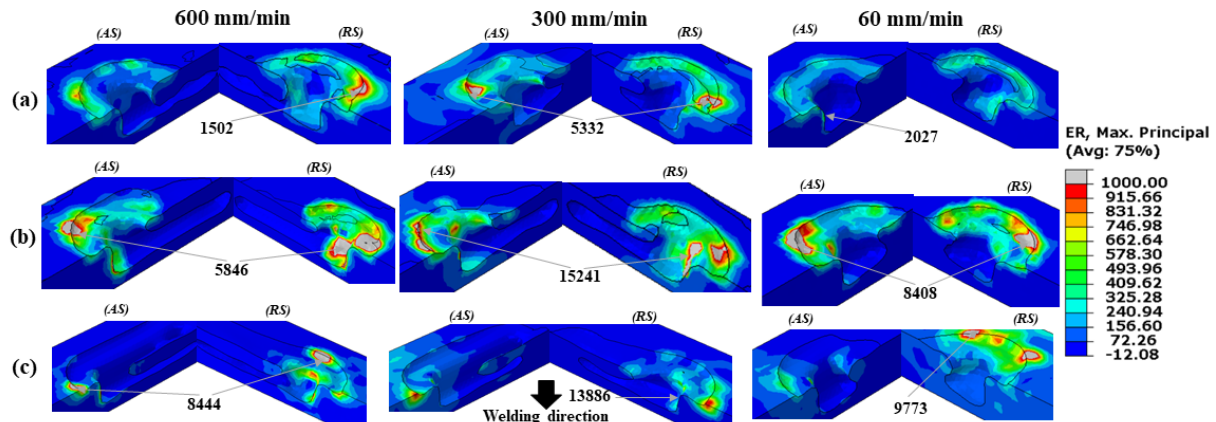


Figure 10: Plastic strain rate around the tool and probe at three traverse speeds for (a) Al-6061-T6, (b) Al-7075-T6, and (c) Al-5083-H18.

#### 4.3 Effect of alloy type on material flow and defect formation

Comparing the three alloys for a given traverse speed, we have seen in Figure 7 the variance in void morphology. The three alloys vary in their chemical composition and thermo-mechanical properties. Re-summarizing the material properties reported earlier, 6061-T6 has the highest thermal conductivity and specific heat, followed by 5083-H18 and 7075-T6. At room temperature, 7075-T6 has the highest tensile and yield strength, whereas 5083-H18 has a considerably higher elevated temperature tensile and yield strength compared to the other two alloys.

For 6061-T6 FSW specimens, the average temperature under the shoulder is close to 570 °C and ranges from 400 °C - 550 °C around the probe, depending on the traverse speed (Figure 9). The least temperatures can be observed corresponding to the void locations in the stir zone. There are a few spots close to the shoulder where the temperature exceeds the solidus (582 °C), and localized melting is observed. Similar variations are observed in the other two alloys. For 7075-T6 alloys, the observed temperatures are above the solidus (477 °C), which has also been reported through experimental measurements [37]. The higher temperatures needed for 7075-T6 alloys can be attributed to the much higher room-temperature tensile properties, requiring more energy to reach the desired strain rates for achieving plastic flow. 5083-H18 alloy, which has a similar solidus temperature to 6061-T6 (580 °C), has lower temperatures in the stir zone compared to the latter, which can be attributed to the higher tensile properties at elevated temperatures. The strain rate maps in Figure 10 show the 7075-T6 alloy to be the most highly strained compared to the other two alloys. Since the thermal conductivity and heat capacity of the 7075-T6 alloy is the lowest, it can convert a higher amount of that heat generation into the plastic flow and increased shearing of the surrounding material. The higher hot strength of the 5053-H18 alloy leads to the lowest strain rates and temperature profiles around the tool probe and the shoulder. This results in the void extending to the tool-workpiece interface and thus forming a groove defect.

Due to the tool geometry, thermal boundary conditions, and asymmetric plastic strain, the material flow in the stir zone during FSW is complex. Fratini et. al. [38] demonstrated the complex flow lines within the stir zone for conditions with and without voids. The flow directions indicate material transferring from the retreating side towards the advancing side of the workpiece. The material underneath the shoulder moves in bulk streams (shoulder-driven flow). As the tool was tilted 2°, a slight vertical material flow was observed on the retreating side. Then it changes direction, moving upward to make ascending laminar flow on the advancing side. Swirl phenomena at the bottom of the weld were

observed, indicating an ineffective material flow and signs of internal tunnel defects due to the material discontinuities [39]. In contrast, material flow at the transverse cross-section of the non-defected weld (shown in Fratini et. al. [38]) is more homogenous with a circular pattern between the advancing side and retreating side, and with no swirl phenomena at the edges.

The material flow was similarly visualized in this work by observing the material velocity vectors (enabled in the Abaqus CEL framework) along with the underlying temperature distribution in the transverse cross-sections of the FSW specimens from numerical simulations (Figure 11). The velocity vectors are shown for the “B-B” cross-section mentioned earlier in Figure 6. This cross-section is taken within the stir zone, right underneath the interface of the FS tool and shoulder. Figure 11-a represents a fully consolidated weld achieved at a traverse speed of 60 mm/min for the 6061-T6 alloy. The velocity vectors follow similar trends to flow vectors shown in Figure 11-b. As mentioned earlier the material underneath the shoulder achieves the maximum temperature close to the solidus and the overall temperature in the stir zone is nearly constant. The velocity vectors show the flow from the retreating side to the advancing side, with material pushed down on the retreating and moving upwards on the advancing side. The circular flow pattern is not observed in the simulations, possibly because of the 0° tool tilt, no eccentricity, runout, and the absence of tool features.

For the traverse speed of 600 mm/min, at which tunnel defects are seen in the stir zone, the velocity flow patterns are in strong agreement with Figure 11-a. The flow pattern near the shoulder is similar to the consolidated weld case; however, in the probe, there are stark differences. Smaller vector vectors are observed around the void, suggesting the absence of flow, and the swirl phenomena, as observed in microstructural observations, are also seen near the bottom of the advancing side. Comparing the same processing condition in the 5053-H18 alloy, which has a groove defect, the swirl phenomenon is also seen at the bottom of the advancing side. The velocity vectors have smaller magnitudes compared to 6061-T6 alloys, suggesting reduced plastic flow which was also observed through the reduced temperatures and plastic strain rates earlier.

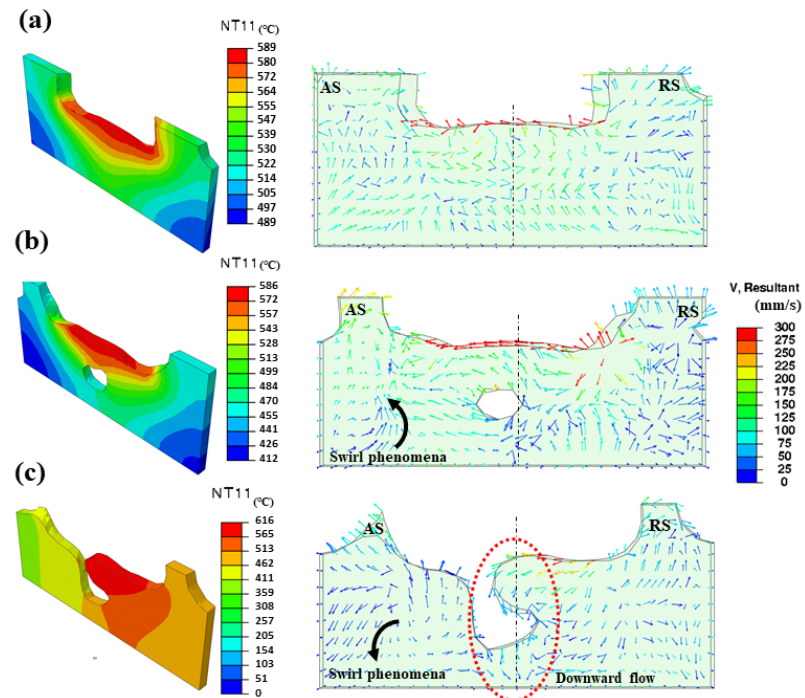


Figure 11: Temperature distribution and material velocity vectors at a transverse cross-section for (a) Al-6061-T6 at 60 mm/min traverse speed, (b) Al-6061-T6 at 600 mm/min traverse speed, and (c) Al-5083-H18 at 600 mm/min traverse speed.

#### 4. Conclusion

This study employs a coupled Eulerian-Lagrangian numerical framework to obtain plastic material flow and temperature distributions that lead to void formation during the FSW process, and to relate the void morphologies to the underlying field distribution and alloy material properties. Three aluminum alloys, viz., 6061-T6, 7075-T6, and 5053-H18 were investigated under varying traverse speeds. The numerical simulations were validated using experimental observations of void morphologies in these three alloys. Temperatures, plastic strain rates, and material flow patterns are considered. The key results and observations from this study are summarized below:

- a) The stir zone and void morphology were in good agreement with the experimental observations. The numerical model can predict void location and size with considerable confidence. For process parameters in the defective regime, tunnel defects were observed for the 6061-T6, and 7075-T6 alloys, whereas the 5053-H18 alloy showed a groove defect.
- b) The temperature and plastic strain rate maps in the steady-state regimen of the process were recorded and showed a strong dependency on the alloy type and traverse speeds. Both temperature and strain rates were higher in the shoulder-driven zone of the stir zone compared to the probe-driven material. The retreating side of the weld showed a higher temperature and strain rate compared to the advancing side.
- c) Due to the higher tensile properties at elevated temperatures for the 5053-H18 alloy, the plastic strain rates and temperatures were least compared to others. Lower thermal conductivity and specific heat of 7075-T6 alloys led to increased shearing (plastic flow) in the stir zone.
- d) The material velocity vectors provided insights into the material flow in the stir zone for both defect and non-defect regimens. When voids are formed, a swirl phenomenon was observed on the advancing side of the probe, with a low magnitude of velocity vectors around the void. Due to the higher elevated tensile properties of the 5053-H18 alloy, the velocity vectors had the least magnitude.

The numerical framework presented here is shown to be useful for predicting different types of defects in aluminum alloys, and potentially in other alloys. Furthermore, the utility of the numerical model for making quantitative predictions and investigating different process parameters and process variables to reduce void formation has been demonstrated. However, many standard assumptions and simplifications intrinsic to the numerical model, with respect to the boundary conditions, material properties, material model, space-time discretization, etc., need to be accounted for when comparing with experimental observations. The model presented here does not consider the compliance of the machine, runout, and eccentricity of the tool. However, these three effects were studied in a recent publication by the authors [23]. It also assumes a rigid tool body and an adiabatic heat condition. As a result, the plunge depth remains consistent in the numerical model, which is not the case in the experiments. In some process conditions, the numerical model overpredicts the process forces, and there are some inconsistencies in the void morphology: The model does not predict voids at 60 mm/min, which were seen in the experiments, and overpredicts the size of voids for 300 mm/min and 600 mm/min compared to the experiments.

As mentioned earlier, the numerical studies and the process signatures (temperature distribution, strain distribution, material flow, and void morphology) studied in this paper are complimentary to a recent publication by the authors in this journal [23], which correlated the process force signals with defect formation and void morphologies. Moving forward, the machine compliance, tool features, tool eccentricity, and runout will be implemented in this numerical framework to make the model more coherent with the experiments.

## Acknowledgments

The authors gratefully acknowledge the financial support for this work from the U.S. National Science Foundation (NSF Grant No. CMMI-1826104), the Department of Mechanical Engineering at the University of Wisconsin-Madison, and colleagues in the Multiscale Metal Manufacturing Processes Lab.

## References

1. Thomas, Wayne M., Edward D. Nicholas, James C. Needham, Michael G. Murch, Peter Temple-Smith, and Christopher J. Dawes. "Friction welding." U.S. Patent 5,460,317, issued October 24, 1995.
2. Leal, Rui M., and Altino Loureiro. "Defects formation in friction stir welding of aluminium alloys." In *Materials Science Forum*, vol. 455, pp. 299-302. Trans Tech Publications Ltd, 2004.
3. Mishra, Rajiv S., and Z. Y. Ma. "Friction stir welding and processing." *Materials science and engineering: R: reports* 50, no. 1-2 (2005): 1-78.
4. Yoshikawa, K. "A joining criterion for lap joining of dissimilar metal materials of aluminum and stainless steel by friction stir." In *The 4th International Symposium on Friction Stir Welding, Park City, Utah, USA*. 2003.
5. Kim, Y. G., H. Fujii, T. Tsumura, T. Komazaki, and K. Nakata. "Effect of welding parameters on microstructure in the stir zone of FSW joints of aluminum die casting alloy." *Materials Letters* 60, no. 29-30 (2006): 3830-3837.
6. Ren, S. R., Z. Y. Ma, and L. Q. Chen. "Effect of welding parameters on tensile properties and fracture behavior of friction stir welded Al-Mg-Si alloy." *Scripta Materialia* 56, no. 1 (2007): 69-72.
7. Chen, Gaoqiang, Han Li, Guoqing Wang, Zhiqiang Guo, Shuai Zhang, Qilei Dai, Xibo Wang, Gong Zhang, and Qingyu Shi. "Effects of pin thread on the in-process material flow behavior during friction stir welding: a computational fluid dynamics study." *International Journal of Machine Tools and Manufacture* 124 (2018): 12-21.
8. Su, Hao, Chuan Song Wu, Marcel Bachmann, and Michael Rethmeier. "Numerical modeling for the effect of pin profiles on thermal and material flow characteristics in friction stir welding." *Materials & Design* 77 (2015): 114-125.
9. Padmanaban, G., and V. Balasubramanian. "Selection of FSW tool pin profile, shoulder diameter and material for joining AZ31B magnesium alloy—an experimental approach." *Materials & Design* 30, no. 7 (2009): 2647-2656.
10. Morisada, Y., T. Imaizumi, and H. Fujii. "Clarification of material flow and defect formation during friction stir welding." *Science and Technology of Welding and Joining* 20, no. 2 (2015): 130-137.
11. Rasti, Javad. "Study of the welding parameters effect on the tunnel void area during friction stir welding of 1060 aluminum alloy." *The International Journal of Advanced Manufacturing Technology* 97, no. 5-8 (2018): 2221-2230.
12. Kim, Y. G., H. Fujii, T. Tsumura, T. Komazaki, and K. Nakata. "Three defect types in friction stir welding of aluminum die casting alloy." *Materials Science and Engineering: A* 415, no. 1-2 (2006): 250-254.
13. Arbegast, W. J., E. R. Coletta, and Z. Li. "Characterization of Friction Stir Weld Defect Types." In *TMS 2001 Annual Spring Meeting, New Orleans, LA*, pp. 11-15. 2001.
14. Agiwal, Hemant, Mohammad Ali Ansari, Daniel Franke, Patrick Faue, Samuel J. Clark, Kamel Fezzaa, Shiva Rudraraju, Michael Zinn, and Frank E. Pfefferkorn. "Material Flow Visualization during Friction Stir Welding using High-Speed X-Ray Imaging." *Manufacturing Letters* (2022).
15. Rosado, Luis S., Telmo G. Santos, Moisés Piedade, Pedro M. Ramos, and Pedro Vilaça. "Advanced technique for non-destructive testing of friction stir welding of metals." *Measurement* 43, no. 8 (2010): 1021-1030.
16. Boldsaikhan, Enkhsaikhan, Edward M. Corwin, Antonette M. Logar, and William J. Arbegast. "The use of neural network and discrete Fourier transform for real-time evaluation of friction stir welding." *Applied Soft Computing* 11, no. 8 (2011): 4839-4846.
17. Shrivastava, Amber, Frank E. Pfefferkorn, Neil A. Duffie, Nicola J. Ferrier, Christopher B. Smith, Kostya Malukhin, and Michael Zinn. "Physics-based process model approach for detecting

- discontinuity during friction stir welding." *The International Journal of Advanced Manufacturing Technology* 79, no. 1 (2015): 605-614.
- 18. Schmidt, Hattel, and Jesper Hattel. "A local model for the thermomechanical conditions in friction stir welding." *Modelling and simulation in materials science and engineering* 13, no. 1 (2004): 77.
  - 19. Al-Badour, Fadi, Nesar Merah, Abdelrahman Shuaib, and Abdelaziz Bazoune. "Coupled Eulerian Lagrangian finite element modeling of friction stir welding processes." *Journal of Materials Processing Technology* 213, no. 8 (2013): 1433-1439.
  - 20. Zhu, Yucan, Gaoqiang Chen, Qilong Chen, Gong Zhang, and Qingyu Shi. "Simulation of material plastic flow driven by non-uniform friction force during friction stir welding and related defect prediction." *Materials & Design* 108 (2016): 400-410.
  - 21. Dialami, Narges, Miguel Cervera, Michele Chiumenti, and Antonio Segatori. "Prediction of joint line remnant defect in friction stir welding." *International Journal of Mechanical Sciences* 151 (2019): 61-69.
  - 22. Ajri, Abhishek, and Yung C. Shin. "Investigation on the effects of process parameters on defect formation in friction stir welded samples via predictive numerical modeling and experiments." *Journal of Manufacturing Science and Engineering* 139, no. 11 (2017).
  - 23. Ansari, Mohammad Ali, Hemant Agiwal, Mike Zinn, Frank Pfefferkorn, and Shiva Rudraraju. "Novel correlations between process forces and void morphology for effective detection and minimization of voids during friction stir welding." *Journal of Manufacturing Science and Engineering* 144, no. 9 (2022): 091007.
  - 24. Johnson, Gordon R., and William H. Cook. "A constitutive model and data for metals subjected to large strains, high strain rates and high temperatures." In *Proceedings of the 7th International Symposium on Ballistics*, vol. 21, no. 1, pp. 541-547. 1983.
  - 25. Soundararajan, Vijay, Srdja Zekovic, and Radovan Kovacevic. "Thermo-mechanical model with adaptive boundary conditions for friction stir welding of Al 6061." *International Journal of Machine Tools and Manufacture* 45, no. 14 (2005): 1577-1587.
  - 26. Brar, N. S., V. S. Joshi, and B. W. Harris. "Constitutive model constants for Al7075-T651 and Al7075-T6." In Aip conference proceedings, vol. 1195, no. 1, pp. 945-948. AIP, 2009.
  - 27. Kim, Dongun, Harsha Badarinarayan, Ji Hoon Kim, Chongmin Kim, Kazutaka Okamoto, R. H. Wagoner, and Kwansoo Chung. "Numerical simulation of friction stir butt welding process for AA5083-H18 sheets." *European Journal of Mechanics-A/Solids* 29, no. 2 (2010): 204-215.
  - 28. HI, GT Gray, Shuh Rong Chen, W. Wright, and M. F. Lopez. "Constitutive Equations for Annealed Metals Under Compression at High Strain Rates and High Temperatures."
  - 29. Kim, Dongun, Harsha Badarinarayan, Ji Hoon Kim, Chongmin Kim, Kazutaka Okamoto, R. H. Wagoner, and Kwansoo Chung. "Numerical simulation of friction stir butt welding process for AA5083-H18 sheets." *European Journal of Mechanics-A/Solids* 29, no. 2 (2010): 204-215.
  - 30. Aval, H. Jamshidi, S. Serajzadeh, and A. H. Kokabi. "Evolution of microstructures and mechanical properties in similar and dissimilar friction stir welding of AA5086 and AA6061." *Materials Science and Engineering: A* 528, no. 28 (2011): 8071-8083.
  - 31. Narendra, Kethireddy, Ammiraju Sowbhagya Madhusudhan Rao, Kalvala Gopal Kishan Rao, and Nallacheruvu Gopi Krishna. "Temperature dependence of density and thermal expansion of wrought aluminum alloys 7041, 7075 and 7095 by gamma ray attenuation method." (2013).
  - 32. Summers, Patrick T., Yanyun Chen, Christian M. Rippe, Ben Allen, Adrian P. Mouritz, Scott W. Case, and Brian Y. Lattimer. "Overview of aluminum alloy mechanical properties during and after fires." *Fire Science Reviews* 4, no. 1 (2015): 3.
  - 33. MatWeb (2018) Material property data. [www.matweb.com](http://www.matweb.com): Aluminum 3003-O, Aluminum 6061-T6; 6061-T651, Aluminum 7075-T6; 7075-T651, Aluminum 2024-T3.
  - 34. Krishnan, K. N. "On the formation of onion rings in friction stir welds." *Materials science and engineering: A* 327, no. 2 (2002): 246-251.
  - 35. Pan, Wenxiao, Dongsheng Li, Alexandre M. Tartakovsky, Said Ahzi, Marwan Khraisheh, and Moe Khaleel. "A new smoothed particle hydrodynamics non-Newtonian model for friction stir welding: Process modeling and simulation of microstructure evolution in a magnesium alloy." *International Journal of Plasticity* 48 (2013): 189-204.
  - 36. Ansari, Mohammad Ali, Avik Samanta, Reza Abdi Behnagh, and Hongtao Ding. "An efficient coupled Eulerian-Lagrangian finite element model for friction stir processing." *The International Journal of Advanced Manufacturing Technology* 101, no. 5-8 (2019): 1495-1508.

37. Cole, E. G., A. Fehrenbacher, N. A. Duffie, M. R. Zinn, F. E. Pfefferkorn, and N. J. Ferrier. "Weld temperature effects during friction stir welding of dissimilar aluminum alloys 6061-t6 and 7075-t6." *The International Journal of Advanced Manufacturing Technology* 71, no. 1-4 (2014): 643-652.
38. Fratini, L., G. Buffa, D. Palmeri, J. Hua, and R. Shivpuri. "Material flow in FSW of AA7075-T6 butt joints: numerical simulations and experimental verifications." *Science and Technology of Welding and Joining* 11, no. 4 (2006): 412-421.
39. Fratini, L., G. Buffa, D. Palmeri, J. Hua, and R. Shivpuri. "Material flow in FSW of AA7075-T6 butt joints: continuous dynamic recrystallization phenomena." (2006): 428-435.Abaqus
40. Abaqus, F.E.A., 2017. Dassault Systemes Simulia Corporation. Providence, Rhode Island, USA.